Materials Science & Engineering A 578 (2013) 115–124

Contents lists available at SciVerse ScienceDirect

Materials Science & Engineering A

journal homepage: www.elsevier.com/locate/msea

Fracture mechanics of stainless steel foams

Sadaf Kashef [a], Alireza Asgari [a,*], Timothy B. Hilditch [a], Wenyi Yan [b], Vijay K. Goel [c], Peter Quadbeck [d], Peter D. Hodgson [e]

[a] School of Engineering, Deakin University, Waurn Ponds, VIC 3217, Australia
[b] Department of Mechanical and Aerospace Engineering, Monash Univesity, Clayton, VIC 3800, Australia
[c] Engineering Center for Orthopaedic Research Excellence, University of Toledo, Toledo, OH 43606, USA
[d] Fraunhofer Institute for Manufacturing Technology and Advanced Materials, Dresden Branch Lab, Dresden 01277, Germany
[e] Institute for Frontier Materials, Deakin University, Waurn Ponds, VIC 3217, Australia

ARTICLE INFO

Article history:
Received 5 February 2013
Accepted 24 March 2013
Available online 19 April 2013

Keywords:
Stainless steel
Cellular metal structures
Fracture toughness
Fatigue crack growth
Modeling

ABSTRACT

The fracture toughness and mode I fatigue crack growth (FCG) tests for open cell stainless steel foam with 45 pores per inch (ppi) have been carried out. In this study, the *R*-curve of crack propagating from a pre-crack was measured for a compact tension specimen by fracture toughness test. The fracture mechanics response was simulated by using an inverted spherical foam modeling approach. The results attained for crack extension rates were described by ΔK, using the Paris-power law approach. The compact tension porous stainless steel specimens have shown full plastic collapse along the ligaments. The microstructure of the foam had a significant influence on the fatigue crack propagation rate. It was found that stainless steel foam has higher Paris exponent than solid stainless steel and the high Paris exponent was explained by crack bridging. The simulation results showed that initiation toughness values strongly depend on failing struts, resulting in cracks that are significantly curved and kinked along their weakest path in stainless steel foam. The results from this study help in predicting and improving mechanical properties of metallic foams with open cell structure.

1. Introduction

Porous stainless steel foams are interesting for functional applications such as catalyst carrier, evaporator, acoustic and thermal insulation. The porous structure of the material makes it possible to achieve extreme low densities, high specific surfaces and in the case of open cell foams, the permeability towards fluids and gases. Porous materials have many voids and flaws because of their porous structure and it is essential to study the fracture mechanics of these materials. Up to this date, studies about fracture toughness and fatigue crack growth rate of these materials and the amount of stress needed to propagate a pre-existing flaw in such materials is limited. In contrast to limited mechanical studies particularly on fracture mechanics of titanium [1,2] and stainless steel foams, there are various studies on titanium foam for biomedical applications [3–5] and also on aluminum foams [6–11]. One example is the study carried out by Combaz et al. [6]. Their study shows that relative density is an important factor in the toughness testing. In porous materials, cracks grow by breaking discrete elements of solid materials [6], which in open cells are usually in the form of struts. The crack propagation in metal foams often occurs by the formation of a plastic yielding around the crack tip. Combaz et al. have carried out fracture toughness of open cell aluminum foams with uniformed cell. They have found that even though their foam fractures with similar physical characteristics to other metal foams, they have higher scaling relation exponent [6]. Motz et al. [7] have studied the fatigue crack propagation in closed cell aluminum and hollow sphere 316L structures. Besides finding high Paris exponent in the closed cell aluminum, they found a continuous fatigue crack growth in this material. However, in the hollow sphere structure, the fatigue crack growth shown to be concentrated in the vicinities of the sintering necks [7].

In general, the fracture toughness of metal foams is dominated by plastic deformation. Therefore, elastic plastic fracture toughness testing is usually conducted using a compact tension specimen [12]. When investigating the fracture mechanics of metal foams, it is important to note that the fracture response of brittle foams is different from ductile foams. In general, brittle foam materials shatter in response to an exterior force, while ductile foam materials only deform. In ductile foams, the coalescence of cavities causes crack nucleation. When ductile foam is loaded, the ductile matrix deforms and the cavities grow larger. Then, the cavities interact with each other, merge and form a crack. Ductile crack growth is much more stable than brittle fracture [13] due to

* Corresponding author. Fax: +61 3 5227 2028.
E-mail address: alireza.asgari@research.deakin.edu.au (A. Asgari).

0921-5093/$ - see front matter © 2013 Elsevier B.V. All rights reserved.
http://dx.doi.org/10.1016/j.msea.2013.03.062

the increasing resistance curve. In elastic plastic fracture mechanics, this is known as *R*-curve behavior showing that resistance to fracture increases as the crack size grows.

In the present work, our aim is to investigate the fracture toughness, fatigue crack growth and material properties of 45 ppi stainless steel foam and analyze the fractured compact tension samples by scanning electron microscopy (SEM) and 3D micro CT scanning.

a	crack length
a_i	crack size at the end of an unloading/reloading sequence
b_i	uncracked ligament size at the end of an unloading/reloading sequence
A_{pl}	area of the plastic deformation in load-displacement diagram
Δa	crack extension
B	specimen thickness
C	power law coefficient
da/dN	crack growth rate
E'	plane strain Young's modulus
EPFM	elastic–plastic fracture mechanics
FCG	fatigue crack growth
J	J-integral (measurement of fracture toughness using EPFM)
J_{IC}	initiation fracture toughness
J_{pl}	J-integral of the plastic deformation
K	stress intensity factor
K_{IC}	plane-strain fracture toughness
ΔK	stress intensity factor range
ΔK_{th}	fatigue crack growth threshold
m	Paris law exponent
N	number of cycles
P	load
P_i	current load during the test
U	displacement
ν	Poisson's ratio
W	width of the specimen
D_c	unit cell diameter
D	inverted solid sphere diameter
K	characteristic length of the model

2. Experimental procedures

2.1. Specimen preparation

Open cell steel foams have been manufactured by using a powder metallurgical replication technique [14]. The method essentially involves three steps: First, a reticulated polyurethane sponge is coated by a metal powder suspension (Atmix 316L, mean powder size 6 μm). Water based slurries with PVA-binder or carbon acid binder and solids content between 87 and 90% were used. In the next step the substrate and the binder are removed by heat treatment (maximum temperature 650 °C), and finally the components are sintered at 1250 °C in hydrogen.

Compact tension stainless steel samples were cut from small panels of $103.50 \times 30.00 \times 30.00$ mm^3 by using wire cut technique. For fracture toughness test, compact tension specimens with sizes of $16.00 \times 15.36 \times 6.40$ mm^3 were cut, while for fatigue crack growth test, compact tension specimens with sizes of $31.25 \times 30.00 \times 5.00$ mm^3 were manufactured in order to obtain required dimension per ASTM E1820-08 (the standard test method for measurement of fracture toughness of metallic materials), and ASTM E647-08 (the standard test method for measurement of fatigue crack growth rates), respectively. The compact tension samples were then pre-cracked as defined in the standards [12,15].

2.2. Fracture toughness test

The fracture toughness testing was performed at room temperature using a MTS servo-hydraulic testing machine (MTS 858) at a displacement rate of 0.01 mm/s, in accordance with the ASTM E1820-08. This test method is for the opening mode (mode I) of loading. In this test method, a fatigue pre-cracked specimen was loaded to induce crack extension. Also a continuous measurement of force versus displacement was done and the resistance curve procedure was used for this experiment [12]. Resistance curve behavior means the fracture toughness increases with crack extension as non-proportional stressing exists in the plastic zone at the tip of the crack [10]. In the present study, the resistance curve J_{IC} was measured using the *R*-curve method. From the load P versus load-line displacement u response of the specimen, the J-integral versus crack extension $\Delta\alpha$ response was calculated and plotted.

The assessment of the J-integral depends on an accurate measurement of the crack growth. A precise measurement of crack growth was carried out by using image processing and compliance techniques. Digital images of the surfaces of the samples were taken during the testing with a camera with speed of about 3 fps (frames per second). Digital images of crack tip growth were taken from both sides of the samples. The images were used in performing the crack growth measurements at different crack extensions and the average of crack length on each side of the sample was used as the crack size. Each measurement was carried out at least three times. Even though polishing the specimen will help in the resolution of the crack tip, this method is not applicable for high porosity metals and therefore polishing was not carried out on the samples. On the other hand, lighting was used during testing to aid in the resolution of the crack tip.

The compliance method, another technique for fracture toughness testing, was carried out according to Section 8 of the standard [12]. Compliance means the ratio of displacement increment to force increment [12]. Compliance was used to measure the crack size by fitting a straight line to the upper linear part of a force–displacement curve. This technique could then be verified by applying optical crack size measurements [12]. To estimate the original crack size, unloading/reloading sequences in a force range from 0.5 to 1.0 times the maximum pre-cracking force is used. At least three unloading/reloading sequences needed to estimate the initial crack size.

2.3. Fatigue crack growth test

Fatigue crack growth testing was carried out at room temperature in accordance with ASTM Standard E647-08, on the same servo-hydraulic test machine as fracture toughness test. Tests were conducted in sinusoidal load control at load ratios (minimum load/maximum load) of $R=0.1$ and $R=0.5$ and frequency of 10 Hz. A single specimen was enough to obtain the desired data and at least five samples were tested for each load ratio [15]. The measurement of the crack propagation has been carried out using image processing and compliance methods.

By image processing technique, the crack size is measured as a function of elapsed fatigue cycles [15]. These data are subjected to numerical analysis to establish the rate of crack growth, which are stated as a function of ΔK. This method is similar to the *"fracture toughness test"* as explained in more details in the previous section. Another recommendation by the standard for such method was to

use reference marks in order to eliminate potential errors due to accidental moves. Photographic grids were used in this study without interrupting the test. It was also suggested that for such methods the average value of the two surface crack lengths of compact tension specimen for calculations of crack growth rate might be used [15].

The compliance method was carried out according to Annex 5 of the standard [15]. This method is the reciprocal of the force–displacement slope normalized for the elastic modulus and specimen thickness [15]. Therefore, the relationship between compliance and crack size has been derived analytically for a number of samples.

3. Simulation procedures

3.1. Inverted spherical model

In the study of open or closed cell foams, the explicit representation and modelling of the actual foam structure is quite complex and impractically expensive and time consuming. There have been many attempts to create simplified pore structure models that achieve reasonable correlation with experimental [16,17]. Assuming that plastic zone size is small compared to the geometric dimensions of the specimen, small scale yielding (SSY) boundary layer models have been used to investigate the effect of void size, shape, morphology and void spacing in the ductile fracture simulations [18,19]. In these types of simulation, the explicit void representation requires very refined finite element meshes that significantly increase the computational costs. In this work, we use a modelling technique based on an inverted spherical approach proposed by Smorygo et al. [20]. Their model, which is mainly presented for structural characterisation and gas permeability analyses of metallic and ceramic foams, is extended and used as a basis for fracture toughness simulation here. The advantage of this method lies in establishing the relationships between the fracture toughness parameters to microstructural features of the foam such as cell size, pore size, strut width and thickness, and cell wall surface area. Using this model, it is possible to explore such relations over a range of strut configurations and porosities that pertain to closed and open cell foams.

The inverted spherical model is created by close packing of an array of spheres. The solid spheres are then inverted to represent the voids in the form of a series of interconnected polyhedral or dodecahedron cells with circular openings. The unit cells are abstracted by only two main independent parameters. The first parameter is the diameter of the hypothetical solid sphere (shown as D in Fig. 1) and the second one is the unit cell diameter (shown as D_c in Fig. 1). The unit cell diameter (D_c) is equal to the distance between centres of neighbouring solid spheres. Depending on the value of characteristic length defined as the ratio, $k = D/D_c$ the inverted spherical model could represent closed or open cell foam structures. When $k < 1$, the foam can have isolated voids to form a closed cell structure. As long as $1 < k < 1.155$, the voids interconnect to form a dodecahedron open-cell structure and when $k > 1.155$, the structure loses continuity of solid. Fig. 1 shows two example structures in which variation in dimension D_c has resulted in open or closed cell structures. All dimensions in this figure are shown as a factor multiplying the unit dimension for the centre to centre sphere spacing parameter (D_c). The hexagon area of the base of the unit cell is $(\sqrt{3}/2)D_c^2$ and the unit cell height is $(2\sqrt{2}/\sqrt{3})D_c$; so, the unit cell volume including the spheres

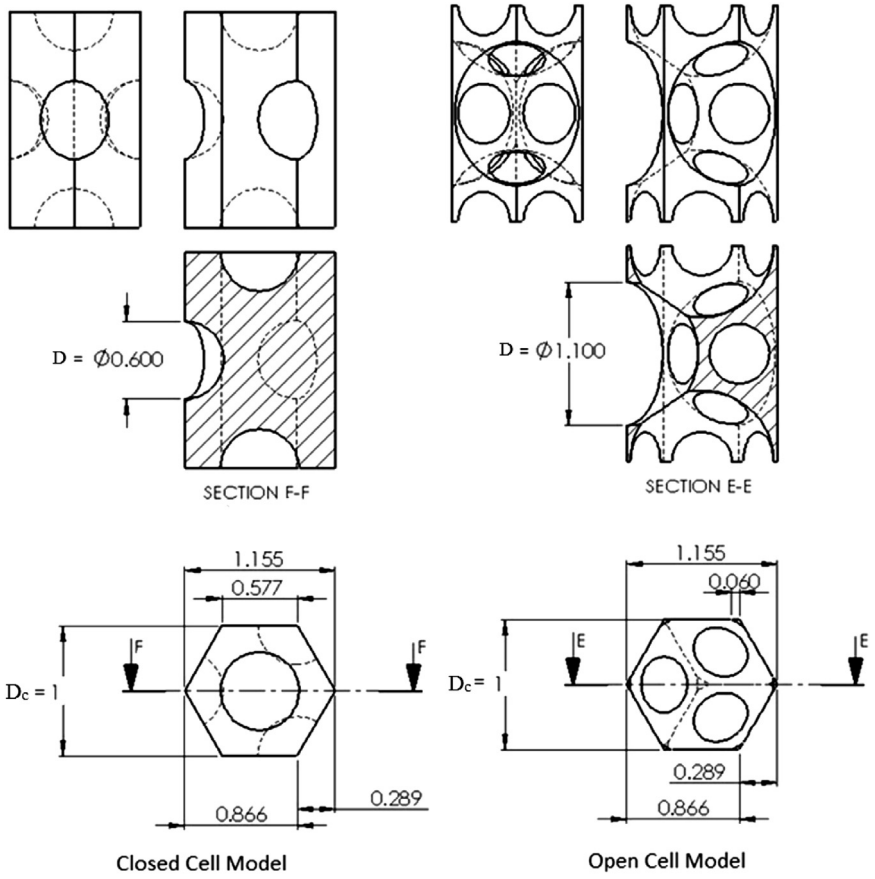

Fig. 1. Inverted spherical models of open cell and closed cell metallic foam, all dimensions are given as a factor of the unit dimension for sphere spacing (parameter D_c shown here).

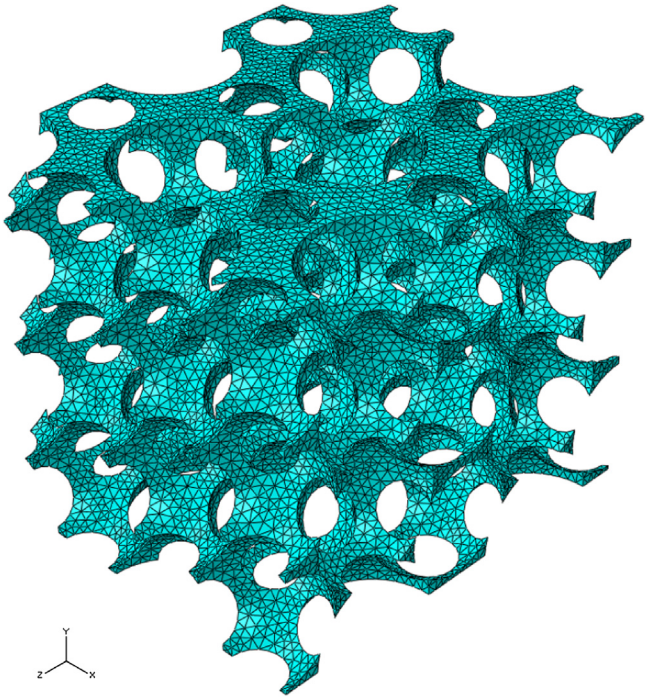

Fig. 2. Inverted spherical FE model of a metallic foam meshed with 92% porosity.

is$V_{pr}=\sqrt{2}{D_c}^3$. For an arbitrary case of dodecahedron open-cell structure ($1<k<1.155$), the volume of complete spheres can be calculated by $V_{sp}=(\pi/3)k{D_c}^3$, which should be adjusted by the intersection between 24 neighbouring spheres; thus, subtracting $V_{adj}=(24\pi/3)((D-D_c)/2)^3((3D/2)-(D-D_c/2))$ from volume of the spheres. The later could be rewritten in terms of the ratio$k$, such that$V_{adj}={D_c}^3(k-1)^2(2k+1)$. The porosity of the open cell foam structure now can be calculated using the following equation [20]

$$\rho=\frac{V_{sp}-V_{adj}}{V_{pr}}=\frac{\pi(k^3-3(k-1)^2(2k+1))}{3\sqrt{2}} \tag{1}$$

The porosity as shown in Eq. (1) is only dependent on the ratio, k, or the spacing between inverted spheres and their diameters. Using this relation, it is possible to create numerical models of foams with a wide range of porosities very efficiently and quickly. As an example, the open cell foam shown in Fig. 2 is 92% porous. The open cell models were used in the fracture toughness simulations of the current study to represent the stainless steel foam open cell structure.

3.2. Macroscale model of stainless steel foam

The macro scale model of this metal foam was created by homogenisation of the unit cell meshed using tetrahedral elements as shown in Fig. 2. The unit cell sizes were $1000\times 1000\times 500$ cube with void sizes of 50 to 200 μm within an orderly dispersed structure simulating only the crack tip region.

In all FE models, the base metal was modelled with typical properties of the austenitic 316L stainless steel by using a power law Ludwigson constitutive equation $\sigma=1354\,\varepsilon^{0.515}$ [21]. For the elastic parameters, Young's modulus was 200 GPa and Poisson's ratio 0.3, and the initial yield stress was taken to be 200 MPa. To study the effect of the pre-crack on the fracture toughness of the model, both conventional finite element modelling and extended finite element method (XFEM) were used to evaluate the J-integral and stress intensity factors of the foam models made by the inverted spherical method. Using conventional finite element and Boolean operations, a sharp edge fatigue pre-crack was induced in the model as shown in Fig. 3a. In this case, no crack propagation and crack growth is possible in the model and instead a cohesive zone modelling technique must be used to predefine the crack path. However, due to the complex micro architecture of the metal foam, the crack propagation path is not known a priori, and only an instant of crack initiation could be modelled. As another option, the XFEM method can be used to create a crack that is able to propagate and grow through the interior of the finite elements. The XFEM seam crack was defined in the bulky region of the model as shown in Fig. 3b to indicate the crack initiation location similar to compact tension specimens. However, the propagation of cracking is not considered in either of two cases and only the onset of cracking in modelled. The maximum principal stress criterion (MAXPS) was used to perform numerical modelling of damage initiation in the XFEM crack.

4. Analysis of fracture toughness results

4.1. Plane strain and initiation fracture toughness

The J_{IC} method is based on the principle of J-integral and characterises the material's toughness close to the commencement of slow-stable crack extension from a pre-existing fatigue crack. The J-integral characterizes an approach to estimate the strain energy release rate per fracture surface area [22]. It is developed to help the complexity involved in calculating the stress near a crack in an elastic–plastic material [22]. In this work, the load is measured during fracture toughness tests as a function of the load-line displacement and J is determined by calculating the area beneath the load–displacement curve by using the following integration

$$J=\frac{2}{Bb}\int_0^u \mathrm{P}\mathrm{d}u \tag{2}$$

At the onset of crack extension, J and J_{IC} are equal [23], as shown in Eq. (3), where U_{cr} is the region underneath the load–displacement curve at the start of crack extension

$$J=\frac{2U}{Bb}\ \text{and}\ J_{IC}=\frac{2U_{cr}}{Bb} \tag{3}$$

Therefore, by just performing one test where the sample was loaded till the start of crack extension, the value of J_{IC} was determined. Normally this is not trivial due to the difficulties of detection of the beginning of the crack extension. The alternative technique is to carry out a number of tests where each sample is loaded to give a small but different crack extension. The multiple specimen method (basic method) forms the basis for the standard J_{IC} test. However, the ASTM E1820-08 allows determination of a true single specimen J_{IC} using the R-curve technique.

Following the standard, the J-integral can be divided into J-integral of elastic and J-integral of plastic (Eq. (4)).

$$J_{total}=J_{elastic}+J_{plastic}=\left[1-(1.0+0.76b_{i-1}/W)\left(\frac{a_i-a_{i-1}}{b_{i-1}}\right)\right]+\left[\begin{matrix}J_{pl(i-1)}\\ +\left(\frac{2.0+0.522b_{i-1}/W}{b_{i-1}}\right)\frac{A_{pl(i)}-A_{pl(i-1)}}{B}\end{matrix}\right]\frac{(K_i)^2(1-\upsilon^2)}{E} \tag{4}$$

The Poisson ratio v is assumed to be 0.3 [24] and, E, the Young's modulus, was found from the elastic unloading compliance technique of the compact tension specimens. The highlighted region in Fig. 4 represents the plastic area increment ($A_{pl(i)}-A_{pl(i-1)}$) for the resistance curve on a load–displacement diagram.

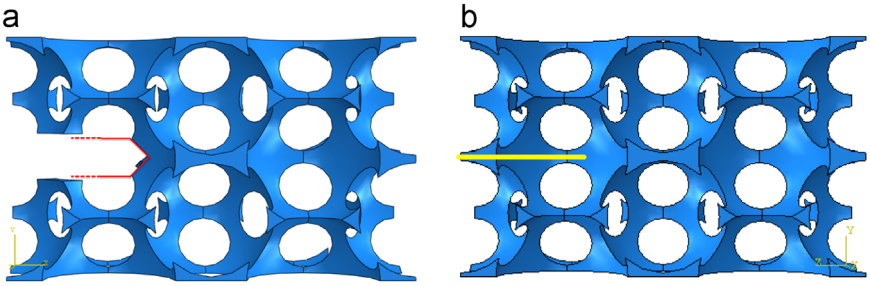

Fig. 3. Side view of an open cell inverted spherical FE model with (a) an induced fatigue pre-crack, and (b) an XFEM crack.

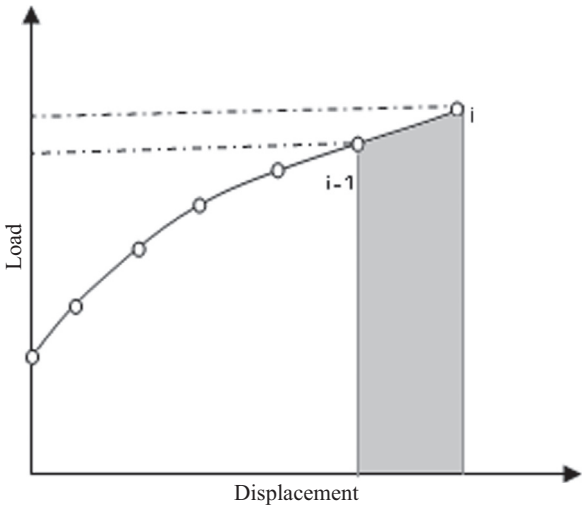

Fig. 4. Load–displacement graph for resistance curve J calculation.

K_i is calculated from

$$K_i = \frac{P_i}{(BW^{0.5})} f(a) \tag{5}$$

P_i is the maximum load, $a = a_i/W$, and

$$f(a) = \frac{(2+a)(0.886 + 4.64a - 13.32a^2 + 14.72a^3 - 5.6a^4)}{(1-a)^{3/2}} \tag{6}$$

The area surrounded by the loading curve, unloading line, and the u-axis (displacement axis) on the P–u (load–displacement) record represents the plastic energy dissipated due to plastic deformation and crack extension where v is displacement between the measurement points and P is force.

J_{IC} is the elastic–plastic failure parameter and is conventionally converted to K_{IC} [12] by using Eqs. (7) and (8).

$$K_{IC} = \sqrt{J_{IC} E'} \tag{7}$$

$$E' = \frac{E}{(1-\nu^2)} \tag{8}$$

The specimens were cyclically unloaded and reloaded during the tests. From the load (P) versus load-line displacement (u) response of the specimen, the J-integral versus crack extension Δa response was calculated and plotted. The unloading/reloading sequence was continued with displacement intervals of 0.005 W or smaller. Before reaching maximum load, at least eight sequences were required. After the final unloading cycle was completed, the force was returned to zero without any additional crosshead displacement.

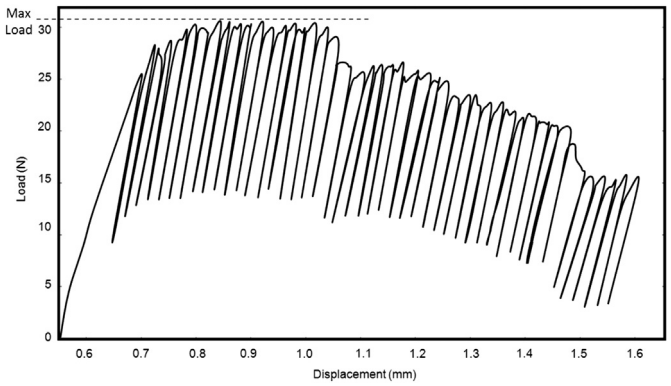

Fig. 5. Load–displacement curve of compact tension stainless steel foam.

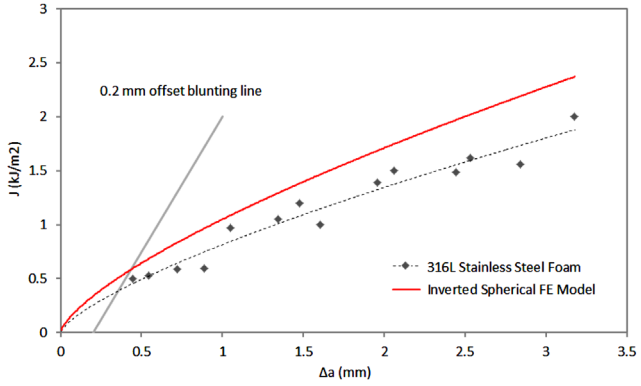

Fig. 6. J-curve for compact tension stainless steel foam with respect to the crack length measurement.

4.2. Load–displacement curve

The stainless steel foam does not have high strength as the base metal does not have a phenomenal strength either. The maximum load used for fracture toughness testing of this foam was 31 N. The load–displacement curve of this metal foam is shown in Fig. 5. The graph shows a sudden drop after the maximum load. At this stage the transition from elastic to plastic deformation occurs. The maximum stress as seen in Fig. 5 corresponds to the upper yield strength (UYS), with no plastic deformation. The load–displacement curve in Fig. 5 displays discontinuous yielding where a rise to an upper yield point follows by a drop to a lower yield point, followed by a rise with an increase in load.

4.3. Fracture response

The plane strain fracture toughness K_{IC} is related to the initiation toughness J_{IC} as was shown in Eqs. (7) and (8). J-integral represents a way to calculate the strain energy release rate per

unit fracture surface area of the material [22]. In Fig. 6, J is plotted vs. $\Delta\alpha$ for stainless steel foam with 45 ppi. The intersection of the curve and the blunting line was taken as the start of the toughness. The cracks blunting lines on the plots are given by Eq. (9), where $\sigma_{ys}\sigma_{pl}$ is the tensile yield strength of the foam.

$$\boldsymbol{J} = 2\sigma_{\boldsymbol{ys}}\Delta\alpha \tag{9}$$

where these blunting lines intercept with the J-curve, J_{IC} is found to be 0.4 kJ/m^2 for porous stainless steel. By using Eq. (7), the plane strain fracture toughness (K_{IC}) is found to be 1.3 MN/m$^{3/2}$. Each measurement was carried out at least three times for each sample within the experimental error of less than 2%. The statistical analysis of the data has shown the degree of error below the 5% confidence level. Therefore, the data are statistically significant.

The J-integral calculated from stress field ahead of crack tip in the inverted spherical FE model is also shown in Fig. 6. The J_{IC} predicted from simulation is slightly higher than the experimental observation but the R curve behavior of the stainless steel foam is clearly captured by the inverted spherical FE model.

In the compact tension samples, plastic bending happens and the ligaments are deformed. Full plastic collapse is noticeable in these samples. In stainless steel foam, the tip of the notch is blunt and broadens and the cut did not progress easily. The cell edges behind the observed crack tip were the main cause of the R-curve behavior. It was assumed the same strain conditions were applied among the ligaments of the foam.

4.4. Micrograph of compact tension samples and fracture toughness behavior

The measured value for Young's modulus E, the initiation toughness J_{IC} from Fig. 6, and the value of plane-strain fracture toughness K_{IC} from Eq. (7) for stainless steel foam are 4.0 GPa, 0.4 kJ/m^2 and 1.3 MN/m$^{3/2}$, respectively. Both X-ray micro computed tomography and SEM were used to study the microstructure of stainless steel foams. Radiographs using computed tomography were recorded using a $1024 \times 1024 \times 1024$ pixel numbers. The total number of projections was 361 with objective magnification of $0.5\times$. Strut structures were inspected at 80 kV X-ray energy level. Fig. 7 shows 3D rendered image of the stainless steel foam with effective voxel size of 25.4 μm. Fig. 7 shows the porous stainless steel foam with homogeneous 45 ppi open pores. The non-uniform crack growth is shown in this 3D image.

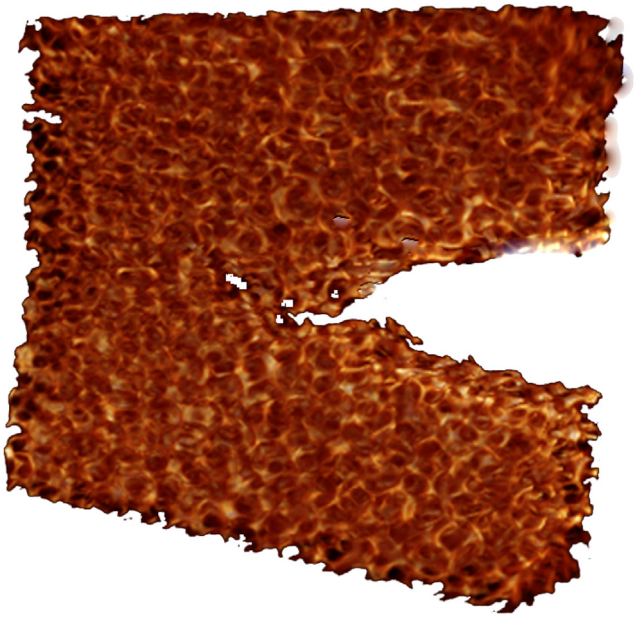

Fig. 7. 3D rendered image of the stainless steel foam after fracture toughness testing.

Fig. 8 shows SEM images of the stainless steel foam with 45 ppi. These images show that ahead of the observed crack tip, the failure of cell edges was apparent. Stainless steel foam made by replication technique has a dodecahedron-like homogeneous pore structure. In stainless steel foam each cell has twelve neighbor and twelve edges [25]. The struts have a smooth surface and triangular shape with concave areas due to the foaming process [25]. In this PM technique, after the heat treatment, the foam resembles the original structure with hollow struts [25]. Change in the shape of the struts and higher density both affect the physical property of the material. In Fig. 8, an edge defect on a strut is shown. This defect is due to incomplete covering of the edge tips and usually occurs in high porous stainless steel foams [25]. Such defects could be reduced by a proper suspension development [26]. Microstructure of the cell struts will affect the macrostructure and the mechanical properties of the stainless steel foam.

At the plastic zone ahead of the crack tip in a cell strut, the micro-cracked area causes the non-linear behavior of the foam material. When the average stress in this zone reaches the cohesive stress, instability happens and the main crack grows in the cell strut [27]. When the local stresses and strains are high enough, voids start to nucleate and grow as the crack blunts [13] and bond with the key crack. The geometric features of the pore arrangements (i.e. cell sizes, spacing morphology) act as a competing mechanism for the crack growth. When plastic deformation happens ahead of the crack tip, crack propagation advances in the weakest zone of deformed porous material. The predictions from finite elements models confirmed that the higher stress concentration on the strut walls exceeds the stress field on a pre-crack induced on the cell walls (Fig. 9). This is shown for crack modeled with both conventional finite element (Fig. 9b) and XFEM (Fig. 9c). The stress field in the material affects the deformation process and the propagating crack of the material [27]. In ductile fracture, usually the crack grows faster at the center of the sample because of the higher stress at that region. The predictions from finite element models show that in all cases, the struts and cell walls are worst-case fatigue and fracture locations. The higher stresses in these locations compete with the main crack tip stress field, which results in diverting and branching of the crack path across several cells ahead of the crack path. This is in line with the experimentally observed R-curve behavior and large scale yielding in the stainless steel foams.

Porosity and thickness of the cell walls have a pronounced effect on the mechanical properties of metal foams [28]. Samples with small pores have higher mechanical strength than metal foams with larger pores. Larger pores offer a greater cell wall length to width ratio. Pore sizes have shown to affect the mechanical properties of the metal foams [29], including the fracture and crack growth of metal foams. Stainless steel foams with thin cell struts fail at lower stresses. As pores stretched in the loading direction, cracks continued from one cell to the next. This led to the crack propagation in the sample. Therefore, the fracture in struts caused the failure in the sample and no sharp crack tip was seen as there were no cell walls. Their ductile behavior has been shown by micro void growth and coalescence at the crack tip. The fracture in cell walls occur randomly from one cell to the next and it follows the weakest path. As soon as the load exceeds the highest strength of the struts, it fails.

The complex loading conditions on the cell walls and struts include shear, tensile and compression which produces cracks that could initiate at the free surface and quickly propagate to the grain boundaries. Depres et al. [30] have shown that the plastic shear zone in the austenitic stainless steel could result in cracks that are

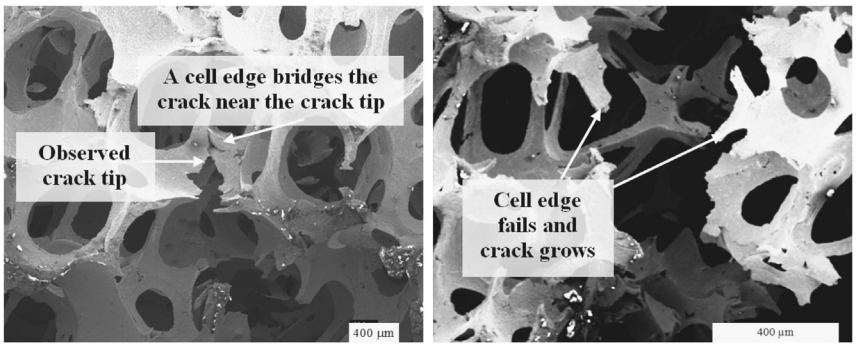

Fig. 8. SEM images of compact tension specimens of stainless steel foams after fracture toughness testing.

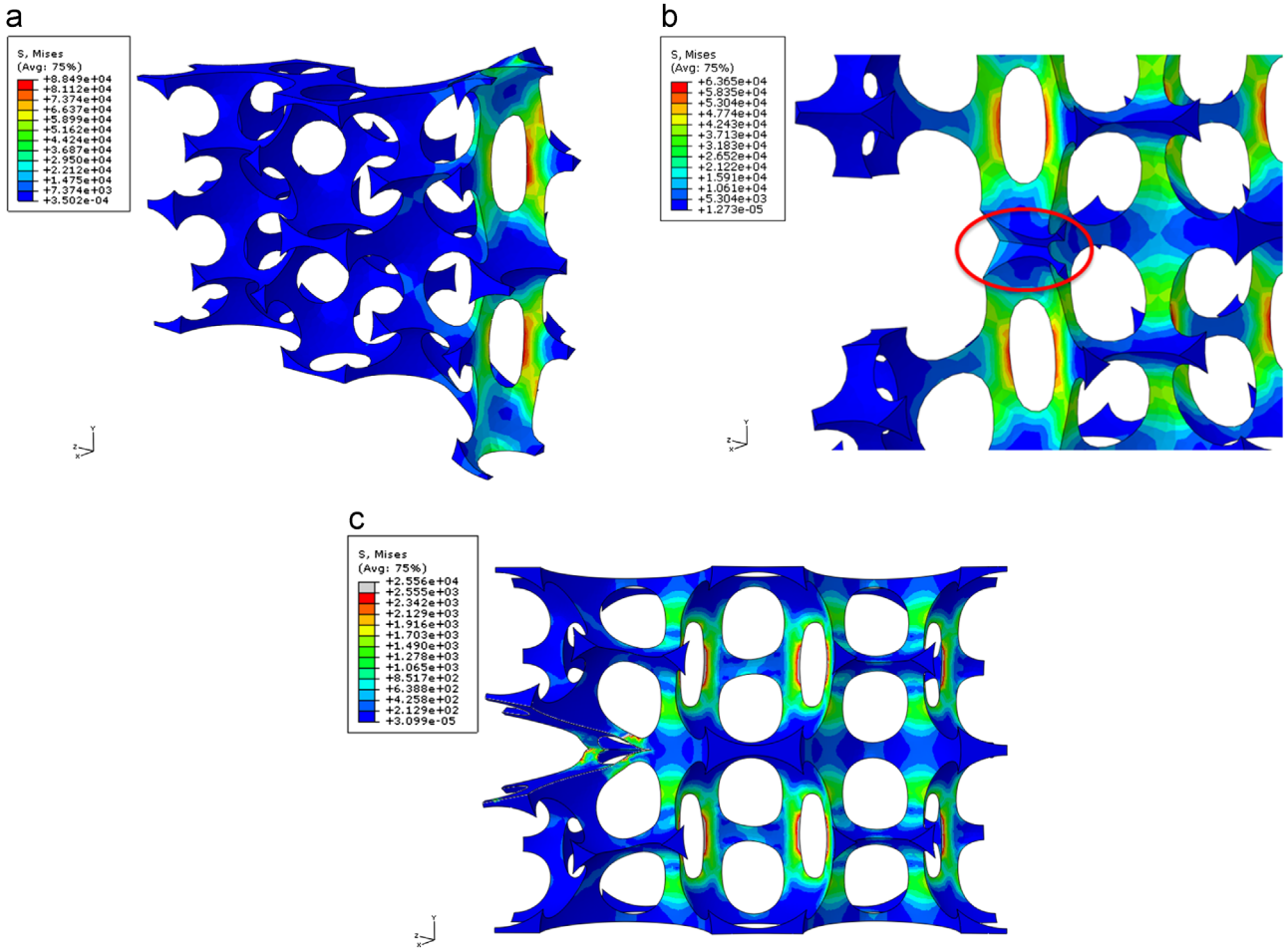

Fig. 9. Stress distribution on the strut and cell walls under localized deformation and damage for (a) the foam without any induced pre-cracks and (b) the foam with an induced pre-crack using conventional finite element and (c) the foam with an induced XFEM crack.

initiated in critical zones of the free surface and grain boundaries assisted by the cross slip and dislocations crossing the free surface. Therefore, the grain boundary separation is the primary source of failure in the struts and cell walls, which is accompanied by plastic deformation and decohesion along the precipitation clusters and other localized defects and inclusions in the base metal.

It was observed that after a peak load, there are some cracks around the edge corners of the notch tip. This is consistent with the findings in closed-cell Alporas and Alulight foams by McCullough et al. and Olurin et al. [8,9].

For our ductile stainless steel foams, we examined whether the Gibson and Ashby's model for fracture toughness of brittle open cell foams is applicable. In addition, the application of McCullough et al. line spring model [8], which was developed for Alulight foams, has been investigated here.

For the line spring model, J_{IC} is found to depend on the area $W(\Delta u)$ under the crack traction versus displacement curve

$$J_{IC} = \frac{2}{\Delta u}\int_0^{\Delta u} W(\Delta u)d\Delta u \tag{10}$$

In the line spring model, the energy absorbed, W, at displacement Δu is [8]

$$W(\Delta u) = \int_0^{\Delta u} T(u)du \tag{11}$$

The proposed crack bridging law defines traction $T(\Delta u)$ based on a reference stress σ_0 and a power law exponent N [8].

$$T(\Delta u) = \sigma_0 \Delta u^N \tag{12}$$

Depending on the value of N, different crack bridging laws could be defined. For example, $N=1$ results in a linear crack bridging law and $N=0$ results in a rigid-ideally plastic limit. This power law relation is chosen for evaluation of J_{IC} in terms of the area ($W(\Delta u)$ under the crack traction versus displacement curve. Therefore, the following equation can be written for J_{IC} [8]:

$$J_{IC} = \frac{2}{N+2} W(\Delta u) \tag{13}$$

Consequently, K_{IC} is found by Eq. (7). For stainless steel foam, the K_{IC} for the line spring model for two power exponents of $N=1$ and $N=0$ and also the predicted K_{IC} from the inverted spherical model presented in this paper are shown in the Fig. 10. The highly porous stainless steel foam studied in this work is represented by a very low density of 0.08 in this figure. The inverted spherical FE model of this paper, and the micromechanical model of Gibson and Ashby, as well as both line spring model predictions with $N=1$ and $N=0$ predict the K_{IC} of stainless steel foam almost very closely at relative density of 0.08. However due to limited data points is not possible to characterize the K_{IC} trend versus relative density of stainless steel foam with only one data point available. Furthermore, there is no data available on the stainless steel foams in literature to give an estimate for K_{IC} of the stainless steel foam at other relative densities. Nevertheless, the fully plastic fracture toughness behavior of this highly porous foam is fully characterized for the relative density of 0.08. Our data combined with the two theoretical models suggests that at very low relative densities, there is very little difference in K_{IC} values despite of the mode of deformation and fracture.

The results obtained in this study on fracture mechanics of 316L stainless steel foam are consistent with the previous studies on the fracture toughness of metallic foams, in which a pronounced R-curve behavior is observed [6,8,9,31]. The suggested failure mechanisms in these cellular metallic materials is of a stable crack growth under large scale yielding condition with a fracture process zone that spans for several cells ahead of the crack tip [6]. The log-log plot of the predicted K_{IC} as a function of relative density is shown in Fig. 11. The predicated data for K_{IC} are related to relative density by changing the two simple geometric features (D and D_c) in the inverted spherical FE model. This log–log plot reveals a slope of 2.3, which is in agreement with the widely accepted model of

$$K_{IC} = C_k \rho^M \tag{14}$$

where C_k and M are material constants with M generally reported to be near 3/2 for cellular metallic foams [6,8,9].

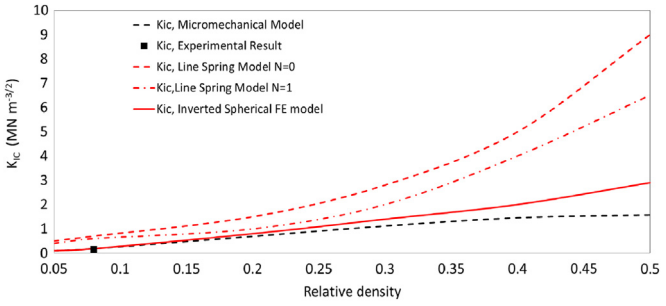

Fig. 10. Comparison of predicted micromechanical model, inverted spherical FE model, and line spring model for 92% porous stainless steel foam.

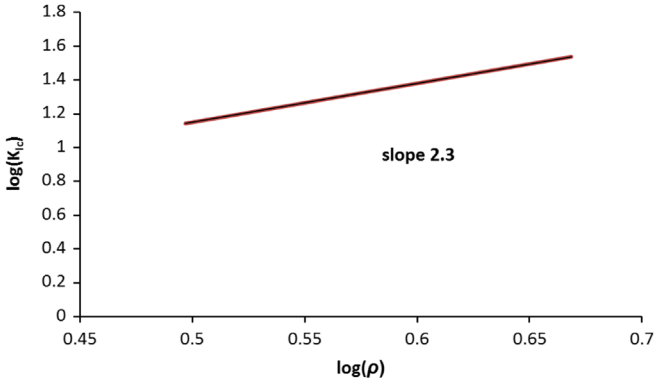

Fig. 11. Calculated K_{IC} as a function of the relative density predicted using the inverted spherical FE model showing a slope of 2.3 in a log–log plot.

5. Analysis of fatigue crack growth test results

5.1. Crack growth rate

The da/dN–ΔK generally has three regions called region I, II and III. Regions I and III are the near-threshold and the rapid-crack propagation regions, respectively. The rates of fatigue crack growth for near threshold (ΔK_{th}) are extremely slow and it takes a while to grow a small crack. In region III, the crack growth rate is extremely high and therefore is called unstable region and obtaining data is quite difficult. Therefore, in this work, region II or Paris region, the stable crack region is considered. This region is defined by a power-law relationship that corresponds to a straight

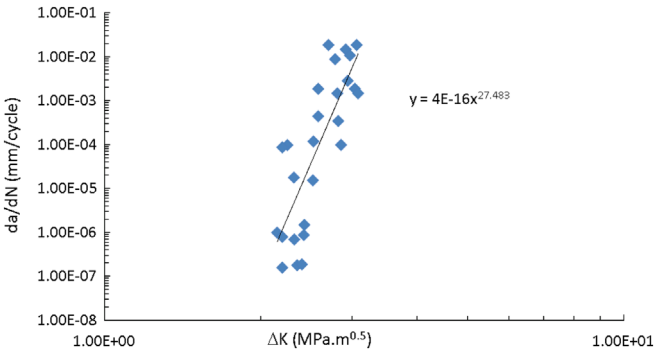

Fig. 12. da/dN–ΔK for 45 ppi stainless steel foam at load ratio of 0.1 using image processing technique.

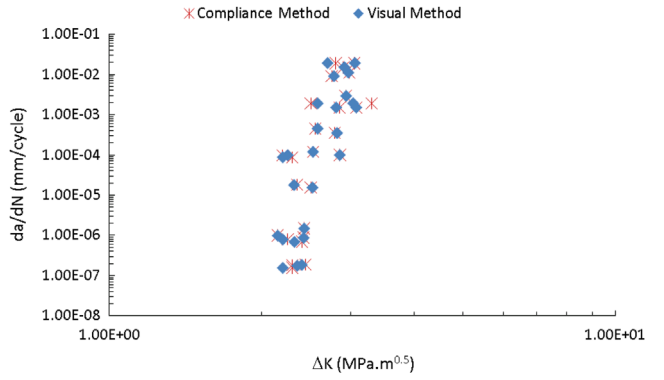

Fig. 13. da/dN–ΔK curve of stainless steel foam using visual and compliance techniques at load ratio of 0.1.

line on a log (da/dN) versus log (ΔK) curve. In this study, the ΔK-increasing test was performed and the fatigue crack growth rate or da/dN was attained from the slope of the a–N curve by following the ASTM E647-08. The crack tip stress intensity factor range, ΔK (K_{max}–K_{min}), was calculated from the maximum and minimum loads of the loading cycles. According to the standard, the measured crack sizes on the front and back of the specimens should not be differing by more than 0.25B, where B is the thickness of the sample. The fatigue crack growth data was expressed in terms of Paris power-law expression, where the Paris law parameters, C and m, are constants

$$\frac{da}{dN} = C\Delta K^m \tag{15}$$

Figs. 12 and 13 show region II, as Paris law only applies to this region. Fig. 12 shows the crack growth rate of a 45 ppi stainless steel foam at load ratio of 0.1 using image processing technique. It was found that the stainless steel foam has a Paris exponent (m) of about 27.5 ± 0.5, which is rather high in comparison to the Paris exponent of 4.9 for solid stainless steel [32]. The values of m were found by curve fitting on experimental data points that have up to 4% maximum experimental error bars.

The rather high Paris exponent in stainless steel foam can be moderately explained by crack bridging. Under tension–tension cyclic loading, a plastic zone is formed at the crack tip due to stress concentration. Crack bridging is found to be a possible explanation of such high Paris exponent in stainless steel foams as crack bridging reduces the crack growth rate and extends the fatigue life.

The da/dN–ΔK data using two different techniques, image processing and compliance methods, are shown for comparison in Fig. 13 at load ratio of 0.1. The results of image processing and compliance methods are in a good agreement.

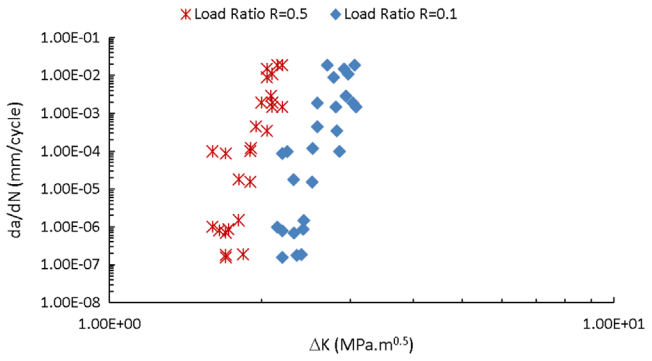

Fig. 14. da/dN–ΔK curve of stainless steel foam using load ratios of 0.1 and 0.5 using image processing technique.

5.2. Effect of different load ratios on the fatigue crack growth (FCG) response

In the present study, specimens were tested with load ratios of $R=0.1$ (lower load ratio) and $R=0.5$ (higher load ratio). It has been shown that the correlation of experimental values for positive ratio of $0 \leq R \leq 1$ is better than for $< R0$ [33] and thus the load ratios of $R > 0$ were chosen for this study. The plots for two different load ratios of 0.1 and 0.5 are shown in Fig. 14 using image processing methods. In this figure, the Paris region for stainless steel foam is shown. It has been established that at the same frequency, with increasing R value, ΔK decreases in consistency with solid metals. For testing at the same frequency and maximum load, it takes longer for the samples at $R=0.5$ to fail than in case of $R=0.1$.

Fig. 15 shows SEM image of stainless steel foam with homogeneous open pores and different pore sizes after FCG testing. Ahead of the observed crack tip, the failure of cell faces is apparent. Fig. 15 shows FCG throughout the porous microstructure and the fracture ligaments. The fracture in cell walls occurs randomly from one cell to the next and it follows the weakest path, which is about the centerline.

The stainless steel foam shows a reasonable fatigue crack growth resistance considering it has such high porosity. Other than crack bridging that reduces the crack growth rate and extends the fatigue life, the foam variables such as the base material, foam density, pore sizes and shapes also affect the crack growth rate [34]. Particularly, the strut thickness and cell wall strength are decisive parameters in terms of crack growth rate. By enhancing the powder coating process, stainless steel foams can be used for a broader range of applications. However, stainless steel foams with mechanical properties studied here could be used as structure material or energy absorption.

5.3. Crack bridging

Crack bridging is a process that reduces the crack growth rate and therefore extends the fatigue life. The growth of the crack bridging zone following the crack tip leads to an increase in crack growth resistance as the crack progresses. Crack bridging was observed in the stainless steel foam samples studied in this work with high Paris exponent. The rather high Paris exponent in the porous stainless steel in the current work can be easily explained by crack bridging. Under tension–tension cyclic loading, a plastic zone is created at the crack tip because of stress concentration. Crack closure was not observed in the stainless steel foam but crack bridging was found to be a possible explanation of such high Paris exponent in these foams. Olurin et al. [9] also found a high Paris exponent for Alulight compared to the solid ductile equivalent material. They found that the fatigue failure of the cell edges behind the crack tip will cause the degradation of crack bridging and this will control the fatigue crack growth rate [9].

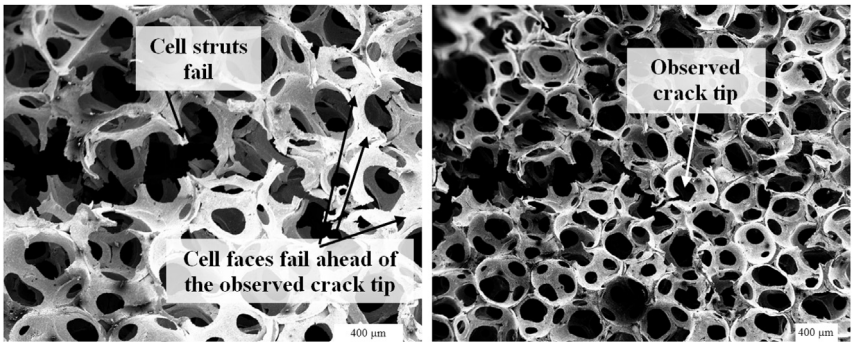

Fig. 15. SEM images of compact tension specimens of stainless steel foam after FCG testing.

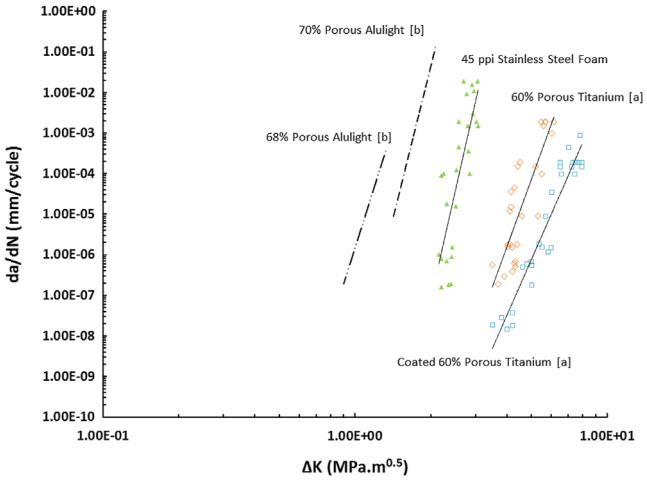

Fig. 16. Comparison of the da/dN–ΔK data of different materials: porous titanium [2], Alulight [9] and stainless steel foam.

5.4. Comparison of FCG rate of stainless steel foam with other metallic foams

While there are significant differences in deformation mechanisms, brittleness or ductile behavior of metal foams, there are similarities in fatigue crack growth behavior of the stainless steel foam with that of other metallic foams described in literature [2,9]. In particular, metallic foam materials shown to have significantly higher m values than solid metals and therefore they are less at risk of failure by crack growth propagation [2], due to crack bridging and closure mechanisms. The da/dN–ΔK values of porous titanium, porous stainless steel and Alulight are shown in Fig. 16. The Paris exponent (m) of stainless steel foam with 92% porosity is 27.5, which is higher than the 60% solid coated porous titanium ($m=14.16$), 60% porous titanium ($m=17.15$) [2], 68% Alulight ($m=24.98$) and 70% Alulight ($m=19.66$) [9].

The Paris exponent of metal foams are reported to be considerably higher than solid metals, nonetheless much lower than Ceramics with high Paris exponent of 50 and above [2]. Ceramics have pores and microcracks and such high Paris exponents in ceramics may be possible due to crack closure, debris or even microcracking and microplasticity [2,35].

6. Conclusions

The mode I fatigue crack growth of stainless steel foam has been measured and explained in terms of microstructure. The compact tension specimens showed full plastic collapse along the ligament. It was concluded that the microstructure of the foam has a significant influence on the fatigue crack growth of stainless steel foam, and this was in agreement with previous studies on fracture behavior of porous aluminum and titanium foams. Stainless steel foam has a higher Paris exponent than solid stainless steel. The high Paris exponent was explained by crack bridging. The tensile stress is lower for low relative density stainless steel foams, because the highly porous microstructure allows struts to deform more easily. Stainless steel foam with 92% porosity has relatively similar fracture behaviour to 60 and 70% aluminium foam. This suggests that while foam porosity is an important factor in mechanical performance of metal foams, the base metal properties and the cell shape and size of the metal foams are also important. An inverted spherical method was used to create explicit geometrical models of the stainless steel foam. The inverted spherical FE model was used to study the onset of cracking by using conventional finite element method and XFEM. In all cases, the failure mechanism predicted by the models suggested and confirmed a strong R-curve behavior. The stainless steel foam offers functional characteristics such as low density, high specific surface, firmness, sound absorption and heat transfer, thus making it suitable for lightweight construction structures, electrodes or thermal insulation elements. Further research would be beneficial to understand the effect of environment and powder coating on the crack growth rate of these stainless steel foams.

Acknowledgement

This work is financially supported by the Australian Research Council (Project No: DP0770021) and ARC grant from ARNAM. The authors also thank David Dick for his support in the E-CORE laboratory at the University of Toledo.

References

[1] S. Kashef, A. Asgari, T. Hilditch, W. Yan, V.K. Goel, P.D. Hodgson, Mater. Sci. Eng., A 527 (29–30) (2010) 7689–7693.
[2] S. Kashef, A. Asgari, W. Yan, V.K. Goel, T. Hilditch, P.D. Hodgson, Mater. Sci. Eng., A 528 (3) (2011) 1602–1607.
[3] C.E. Wen, M. Mabuchi, Y. Yamada, K. Shimojima, Y. Chino, T. Asahina, Scr. Mater. 45 (2001) 1147–1153.
[4] C.E. Wen, Y. Yamada, A. Nouri, P.D. Hodgson, Mater. Sci. Forum 539–543 (2007) 720–725.
[5] C.E. Wen, Y. Yamada, K. Shimojima, Y. Chino, H. Hosokawa, M. Mabuchi, J. Mater. Res. 17 (10) (2002) 2633–2639.
[6] E. Combaz, A. Mortensen, Acta Mater. 58 (2010) 4590–4603.
[7] C. Motz, O. Friedl, R. Pippan, Int. J. Fatigue 27 (2005) 1571–1581.
[8] K.Y.G. McCullough, N.A. Fleck, M.F. Ashby, Acta Mater. 47 (8) (1999) 2331–2343.
[9] O.B. Olurin, K.Y.G. McCullough, N.A. Fleck, M.F. Ashby, Int. J. Fatigue 23 (2000) 375–382.
[10] C. Chen, N.A. Fleck, T.J. Lu, J. Mech. Phys. Solids 49 (2001) 231–259.
[11] J. Banhart, Prog. Mater. Sci. 46 (2001) 559–632.
[12] A., Standard Test Method for Measurement of Fracture Toughness, ASTM International, West Conshohocken, PA, USA48 E1820-08.
[13] T.L. Anderson, Fracture Mechanics: Fundamentals and Applications, CRC Press, 1995.
[14] IFAM. Annual Report Dresden, Germany: Fraunhofer Institute for Manufacturing Technology and Applied Materials Research, 2005.
[15] A., Standard Test Method for Measurement of Fatigue Crack Growth Rates, ASTM International, West Conshohocken, PA45 E647-08.
[16] J.G. Fourie, J.P. Du Plessis, Chem. Eng. Sci. 57 (2002) 2781–2789.
[17] J. Despois, A. Mortensen, Acta Mater. 53 (2005) 1381–1388.
[18] J. Kim, G. Zhang, X. Gao, Int. J. Solids Struct. 44 (2007) 1844–1862.
[19] J.P. Petti, R.H. Dodds Jr., Int. J. Solids Struct. 42 (2005) 3655–3676.
[20] O. Smorygo, V. Mikutski, A. Marukovich, A. Ilyushchanka, V. Sadykov, A. Smirnova, Acta Mater. 59 (2011) 2669–2678.
[21] K.G. Samuel, P. Rodriguez, J. Mater. Sci. 40 (2005) 5727–5731.
[22] H. Tada, P.C. Paris, G.R. Irwin, (Eds.), The Stress Analysis of Cracks American Society of Mechanical Engineers, 2000.
[23] M. Janssen, J. Zuidema, R. Wanhill, Fracture Mechanics, second ed, Spon Press, New York, 2004.
[24] M.F. Ashby, A.G. Evans, N.A. Fleck, L.J. Gibson, J.W. Hutchinson, H.N.G. Wadley, Metal Foams: a Design Guide, Butterworth-Heinemann, Woburn, MA, USA, 2000.
[25] P. Quadbeck, G. Stephani, K. Kummel, J. Adler, G. Standke, Mater. Sci. Forum 534–536 (2007) 1005–1008.
[26] P. Quadbeck, K. Kummel, R. Hauser, G. Standke, J. Adler, G. Stephani. Open cell metal foams—application-oriented structure and metal selection, in: CELLMAT 2010, 2010, pp. 279–288.
[27] M. Sahimi, Heterogeneous Materials I, Springer, USA, 2003.
[28] M.S. Aly, Y. Fukasawa, K. Morishita, H. Okuda, S. Ochiai, K. Kato, K. Kita, K. Honma, in: L.P. Lefebvre, J. Banhart, D.C. Dunand (Eds.), MetFoam 2007: Porous Metals and Metallic Foams, DEStech Publications, Inc., Lancaster, PA, 2007, pp. 157–160.
[29] T.G. Nieh, K. Higashi, J. Wadsworth, Mater. Sci. Eng., A A283 (2000) 105–110.
[30] C. Depres, C.F. Robertson, M.C. Fivel, Mater. Sci. Eng., A 387–389 (2004) 288–291.
[31] Y. Sugimura, J. Meyer, M.Y. He, H. Bart-Smith, J. Grenstedt, A.G. Evans, Acta Mater. 45 (12) (1997) 5245–5259.
[32] A.C. Pickard, R.O. Ritchie, J.F. Knott, Metall Tech 2 (1975) 253–263.
[33] A.H. Noroozi, G. Glinka, S. Lambert, Int. J. Fatigue 27 (2005) 1277–1296.
[34] S. Kashef, W. Yan, J. Lin, P.D. Hodgson, Mod. Phys. Lett. B 22 (2008) 6155–6160.
[35] S. Li, L. Sun, W. Jia, Z. Wang, J. Mater. Sci. Lett. 14 (1995) 1493–1495.